Journal of Applied Fluid Mechanics, Vol. 18, No. 4, pp. 960-975, 2025.
Available online at www.jafmonline.net, ISSN 1735-3572, EISSN 1735-3645.
https://doi.org/10.47176/jafm.18.4.2937

Comprehensive Research on the Effects of Different Launch Conditions on Pump-jet Propulsor Performance

Q. Fu†, Y. Duan, W. Shi, H. Li and R. Zhu

National Research Center of Pumps, Jiangsu University, Zhenjiang, Jiangsu, 212013, China

†*Corresponding Author Email: fuq@ujs.edu.cn*

ABSTRACT

This paper compares the cavitation of a pump-jet propulsor under different launch conditions and discusses the effects of cavitation on the performance and noise of the pump-jet propulsor rotor blade. At the same time, the load and deformation of the rotor blade under the conditions of cavitation are studied via the one-way fluid-structure interaction (FSI) approach. The results show that the cavitation of the pump-jet propulsor decreases with increasing launch depth and speed. The performance decreases with increasing launch speed at large depths, whereas the performance improves with increasing launch speed at small depths due to the improvement of the cavitation on the rotor blades. Increasing launch speed and depth increase the noise caused by the rotor of the pump-jet propulsor, and the increase in flow rate caused by the improvement of cavitation also increases the noise level. Moreover, increasing launch depth increases the overall load of the blade and produces a larger deformation, while the speed affects the distribution of the load on the blade. In addition, with the improvement of cavitation caused by increasing launch speed, the deformation of the blade decreases.

Article History

Received June 23, 2024
Revised September 28, 2024
Accepted October 20, 2024
Available online February 4, 2025

Keywords:

Pump-jet propulsor
Cavitation
Vortex
Noise
Fluid-structure interaction

1. INTRODUCTION

With the wide application of pump-jet propulsors in various types of vehicles, their hydrodynamic performance, cavitation performance and acoustic performance under different working conditions and structures have become important research topics. Researchers worldwide have conducted studies on problems arising in engineering.

The hydrodynamic and cavitation performance of pump-jet propulsors is a primary concern for researchers. Qiu et al. (2020a) reported that inlet angles have more significant effects than rotor tip clearances do on cavitation and pressure pulsations. Qiu et al. (2020b) further investigated the influence of the inlet angle and speed ratio on the excitation force. Lu et al. (2020) reported a substantial decline in performance and intense vibrations when the inlet angle exceeded 20 degrees. Q. Huang et al. (2022) shifted their focus to the influence of oblique inflow on the pump-jet slipstream, whereas Sun et al. (2022) discussed the impact of slipstream inclination on performance under oblique flow conditions. Qin et al. (2021a) highlighted the influence of the tail vortex on the slipstream. Zhao et al. (2022) revealed that interactions between stator and rotor trailing edge vortices and blade cavitation accelerate the breakdown of the downstream vortex system. Gan et al. (2023) examined the hydrodynamic and cavitation performance of pump-jet thrusters by altering the inlet flow rate. Research by Al-Obaidi (2023, 2024a) revealed the significant effects of the tip vortex flow on the internal flow and pressure fluctuations in axial pumps, particularly under low water level conditions, where it results in substantial pressure pulsations and backflow at the blade tip clearance. A collaborative study led by Al-Obaidi et al. (2023a, 2024) indicated that operating conditions play a decisive role in the characteristics of the flow field, with blade tip deviation being essential for the stable and safe operation of the pump. These studies also emphasize that understanding the flow distribution, especially the influence of the tip blade on flow patterns and performance, is vital for improving the design and production of axial pumps.

Research has also focused on the impact of various pump-jet structures. Xu and Lai (2023) delved into the effect of the installation sequence on the cavitation performance, and Qin et al. (2021b) elucidated the influence on the tail vortex characteristics. Yuan et al. (2020) and Li et al. (2020) utilized DES turbulence modeling to analyze the blade tip-clearance dynamics,

NOMENCLATURE

p	pressure	$H(f)$	Heaviside generalized function
u	velocity	us	structural displacement
ρ	density	D	structural stiffness matrix
μ	viscosity	fs	forces
a	phase volume fraction	Q_0	design flow rate
l	liquid phase	η	design efficiency
v	vapor phase	D_{rs}	rotor shroud diameter
R_B	radius of the bubble	H_D	launch depth
r_{nuc}	volume size of the vapor nucleus	V_K	launch speed
p_V	saturated vapor pressure	P_T	test standard pressure
c_0	far-field sound speed	P_∞	inlet steady flow pressure
p'	sound pressure value	U_∞	inlet steady flow velocity
$\delta(f)$	Dirac delta function	J	advance coefficient
n_j	unit outward normal vector	KTr	thrust coefficient
T_{ij}	Lighthill stress tensor	SPL	sound pressure level

revealing the interplay between cavitation and vortices. Lu et al. (2016) and Q. Huang et al. (2021) explored the impact of tip clearance on performance and cavitation. Ye et al. (2022) introduced circumferential axial slots to mitigate the detrimental impact of tip vortices.

Noise and structural strength are vital during pump-jet operation. Shi et al. (2022) compared flow noise with structural noise and concluded that structural noise is more dominant at low speeds. An et al. (2020, 2023) meticulously examined fluid–blade interactions under varying conditions and suggested the use of composite materials. Xiong et al. (2022) and X. Huang et al. (2021) analyzed the effect of turbulence on noise. Li et al. (2023) investigated the effects of a pre-swirl stator on the radiation noise characteristics. Yang et al. (2024) and Guo et al. (2022) introduced wave-shaped or sawtooth-shaped structures to reduce noise during operation. Al-Obaidi (2018, 2019, 2024b) successfully implemented early detection and diagnosis of cavitation in centrifugal pumps by integrating acoustic, vibration analysis, and CFD techniques and estimated cavitation levels through time–frequency domain signal analysis, thereby increasing pump reliability, extending service life, and providing detailed preventive information to avoid system shutdowns. Al-Obaidi et al. (2024) utilized CFD to investigate the internal flow and pressure fluctuations in axial pumps at various blade angles for performance optimization, with the findings showing good agreement between the numerical predictions and experimental results. In further research, Al-Obaidi and Alhamid (2023, 2024) discovered that the blade angle and quantity significantly impact the flow dynamics and the causes of vibration.

These comprehensive studies have shed light on the intricate interplay between various factors and pump-jet propulsor performance. However, most of the articles focus on research during the cruising process, whereas research on pump-jet propulsors during launch or delivery to the cruising phase is rarely heard of. This paper studies the performance of a pump-jet propulsor during launch at different velocities and depths, reaching a set rotational speed, with a focus on performance, noise, and blade load, to support research on launch strategies and optimization.

2. NUMERICAL CALCULATION METHOD

The approach presented in this paper integrates computational fluid dynamics (CFD) with specialized acoustic and structural modules. This methodology is utilized to perform numerical simulations of pump-jet propulsors across a range of launch depths and speeds, as illustrated in the detailed flowchart in Fig. 1.

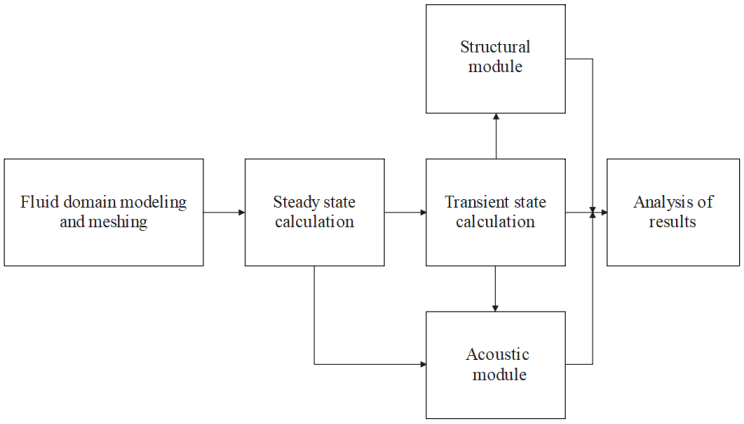

Fig. 1 Flow chart of the numerical simulation methodology

2.1 Governing Equations

In this work, owing to the numerical calculation of the cavitation condition (Goossens & Goossens, 2003), the momentum and mass equations of the fluid are as follows:

$$\frac{\partial \rho_m}{\partial t}+\frac{\partial(\rho_m u_i)}{\partial x_i}=0 \tag{1}$$

$$\frac{\partial(\rho_m u_j)}{\partial t}+\frac{\partial(\rho_m u_j u_i)}{\partial x_i}=-\frac{\partial p}{\partial x_j}+\frac{\partial}{\partial x_i}\left(\mu_m \frac{\partial u_j}{\partial x_i}\right) \tag{2}$$

where p is the pressure, u is the velocity, the subscripts i and j denote the components of the quantity in different directions, ρ represents the density of the working medium, μ represents the viscosity of the working medium under working conditions, and the subscript m of ρ and μ indicates that the quantities refer to a mixture. The numerical value after mixing can be determined via the following formula:

$$\rho_m=\alpha_l\rho_l+(1-\alpha_l)\rho_v \tag{3}$$

$$\mu_m=\alpha_l\mu_l+(1-\alpha_l)\mu_v \tag{4}$$

where a is the volume fraction of the phase, the subscript l represents the liquid phase and v represents the vapor phase.

2.2 Turbulence Equation

In this study, we utilize the SST-based improved delayed detached eddy simulation (IDDES) model for numerical computations. This method is a hybrid of the RANS and LES techniques, striking a balance between computational demands and accuracy. It has been extensively applied in the numerical simulation of rotating machinery in recent years. For example, Krappel et al. (2015) employed the IDDES model for numerical computations of a pump turbine, and Ren et al. (2019) utilized it to simulate the flow within the impeller of a centrifugal pump. The governing equations of the model are as follows:

$$\frac{\partial(\rho k)}{\partial t}+\nabla\cdot\left(\rho\vec{U}k\right)=\nabla\cdot\left[(\mu+\sigma_k\mu_t)\nabla k\right]+P_k-\frac{\rho\sqrt{k^3}}{l_{IDDES}} \tag{5}$$

$$\frac{\partial(\rho\omega)}{\partial t}+\nabla\cdot\left(\rho\vec{U}\omega\right)=\nabla\cdot\left[(\mu+\sigma_\omega\mu_t)\nabla\omega\right]+\alpha\frac{\rho}{\mu_t}P_k+2(1-F_1)\rho\sigma_{\omega2}\frac{\nabla k\cdot\nabla\omega}{\omega}-\beta\rho\omega^2 \tag{6}$$

$$\mu_t=\rho\frac{\alpha_1\cdot k}{\max(\alpha_1\cdot\omega,F_2\cdot S)} \tag{7}$$

Here, F_1 and F_2 denote the SST mixing function, and P_k is the generation term of k. The length scale of IDDES in Equation (5) is as follows:

$$l_{IDDES}=\tilde{f}_d\cdot l_{RANS}+(1-\tilde{f}_d)\cdot l_{LES} \tag{8}$$

l_{RANS} and l_{LES} are the turbulence length scales of the RANS and LES models, respectively, which need to be calculated via the empirical mixing equations. All the above equations and the parameters can be further solved according to Gritskevich et al. (2012).

In this study, to alleviate the computational load and meet the convergence and stability requirements, we perform initial steady-state calculations via the SST k-ω turbulence model. Once numerical stability is achieved, we then transition to transient calculations employing the SST-based IDDES model.

2.3 Cavitation Equation

The Zwart-Gerber-Belamri (Z-G-B) cavitation model is employed in this research (Zwart et al., 2004). Owing to its widespread application in propeller cavitation simulations, it has been selected to investigate the cavitation characteristics of pump-jet propulsors. The condensation and evaporation equations of this model are as follows:

$$m^+=F_e\frac{3r_{nuc}(1-\alpha_V)\rho_V}{R_B}\sqrt{\frac{2(p_V-p)}{3\rho_l}},\ p<p_V; \tag{9}$$

$$m^-=F_c\frac{3\alpha_V\rho_V}{R_B}\sqrt{\frac{2(p_V-p)}{3\rho_l}},\ p<p_V; \tag{10}$$

In the equations, m^+ and m^- denote the rates of evaporation and condensation, respectively. F_e and F_c are the coefficients for evaporation and condensation, respectively. R_B represents the radius of the bubble, and r_{nuc} is the volume size of the vapor nucleus. P_v is the saturated vapor pressure, which varies with temperature.

2.4 Ffowcs Williams–Hawkings Acoustic Equation

The Ffowcs Williams–Hawkings (FW–H) equation has been widely applied in the field of noise prediction (Ffowcs Williams & Hawkings, 1969). It extracts equivalent acoustic sources from nonlinear flow fields and decouples the computation of the flow field from the acoustic field, thereby simplifying the problem. The specific equation is as follows:

$$\left(\frac{1}{c_0^2}\frac{\partial^2}{\partial t^2}-\frac{\partial^2}{\partial x_i\partial x_j}\right)p'=\frac{\partial\{[\rho_0 v_n+\rho(u_n-v_n)]\delta(f)\}}{\partial t}+\frac{\partial^2\left(T_{ij}H(f)\right)}{\partial x_i\partial x_j}-\frac{\partial\{[P_{ij}n_j+\rho u_i(u_n-v_n)]\delta(f)\}}{\partial x_i} \tag{11}$$

where c_0 represents the far-field sound speed in the fluid medium; p' represents the sound pressure value at the observation point at time t; ρ represents the fluid density; ρ_0 represents the density of the fluid in the far field; u_i represents the fluid velocity component in the x_i direction; u_n and v_n represent the fluid velocity and source surface velocity components perpendicular to the source surface, respectively; $\delta(f)$ represents the Dirac delta function; P_{ij} represents the stress tensor; n_j represents the unit outward normal vector on the control surface; T_{ij} represents the Lighthill stress tensor; and $H(f)$ represents the Heaviside generalized function. The three terms on the right-hand

side of the equation represent the monopole source, dipole source, and quadrupole source.

2.5 Coupling Method

In the coupling of blades with fluid, the basic governing equation of the fluid–structure interaction is as follows:

$$\rho_s \frac{\partial^2 u_s}{\partial t^2} + D u_s = f_s \tag{12}$$

Here, ρ_s is the density of the structure, u_s is the structural displacement, D is the structural stiffness matrix, and f_s represents the forces acting on the structure, including those from the fluid and other external forces (Dowell & Hall, 2001).

3. RESEARCH OBJECT AND MESHING

To conduct numerical computations for a pump-jet propulsor, it is necessary to simulate its placement within a defined area of water. This chapter focuses primarily on modeling the pump-jet propulsor, mesh generation, and the setup of boundary conditions.

3.1 Parameters and Modeling

A pump-jet propulsor operates by accelerating and pressurizing the working medium within a conduit and then directing it through a tail nozzle to create a high-velocity, high-pressure jet of water that is ejected toward the rear of the vehicle. This action utilizes the reactive force of the working substance to propel the vehicle forward (McCormick & Elsenhuth, 1963). The pump-jet propulsor studied in this paper is based on an axial flow pump design and has the ability to reach high rotational speeds. The pump-jet propulsor features a configuration with four inlet chambers, with the propulsion section mounted at the stern of an underwater vehicle. The array of the inlet chamber is positioned on the surface of the navigational body. The main design parameters of the pump-jet propulsor are shown in Table 1.

In this work, the pump-jet propulsor is mounted on a cylindrical body that is 10 times longer than the rotor shroud diameter D_{rs}. The plane of the cylinder's head section is set as the inlet plane for the water domain, thereby eliminating the effects of turbulence and cavitation caused by the underwater vehicle's bow. The propulsion section of the pump-jet propulsor is depicted in Fig. 2.

Table 1 Main performance parameters and structural parameters of the pump-jet propulsor

Parameter	Value
Design flow rate, Q_0 (kg/s)	531
Design efficiency, η (%)	72
Rotor shroud diameter, D_{rs} (mm)	168
Number of rotor blades	3
Number of stator blades	5
Rotor tip-clearance (mm)	0.2

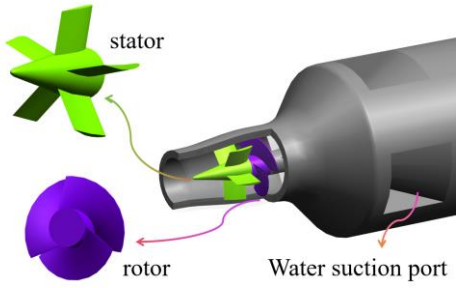

Fig. 2 Main structure of the pump-jet propulsor

3.2 Meshing and Boundary Settings

This paper employs a fully structured mesh model, dividing the overall grid into five parts: the sea region, the inlet chamber, the rotor, the stator, and the nozzle. Interface boundaries are set at the junctions between these parts. For the sections with blade structures, Ansys Turbogrid was used for structured meshing, whereas the other parts were meshed via ICEM. The inlet chamber section was first meshed individually and then replicated and combined into a full row. Figure 3 shows the grids and boundary condition settings for the pump-jet propulsor within the sea region.

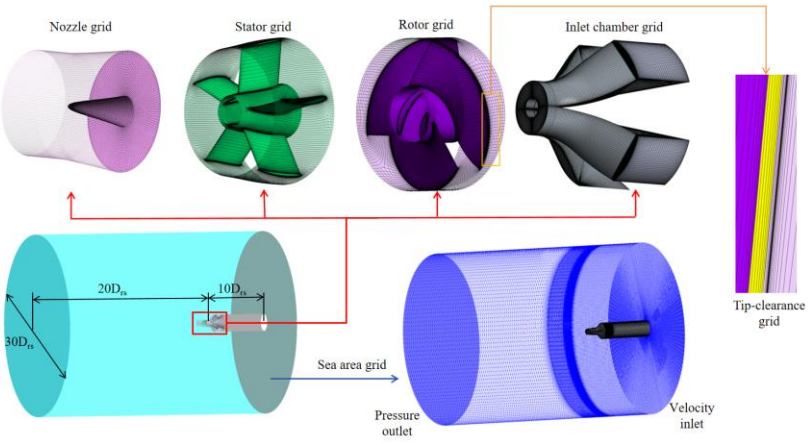

Fig. 3 Grids and boundary conditions

Table 2 Grid independence verification

internal flow field cells （million）	external flow field cells （million）	Current head /Initial head	Current torque /Initial torque
1.21	4.62	1.000	1.000
2.29	4.62	1.036	1.039
2.29	5.80	1.055	1.057
2.88	5.80	1.082	1.083
2.88	6.35	1.083	1.083
3.29	6.35	1.083	1.083

In the figure, the center of rotation of the rotor is set as the origin of the working coordinate system. The distance from the inlet to the center of rotation is 10 times the diameter of the inlet, whereas the distance from the outlet to the origin is 20 times D_{rs}. The entire sea region is a cylinder with a diameter of 30 times D_{rs}. For the boundary conditions, a total of five groups of interface boundaries are set. The walls of the rotor blades and the hub are designated as rotating surfaces. The numerical computations are conducted via the sliding mesh method for the overall model. In this research, the external flow field (sea region) and the internal flow field (from the inlet chamber to the nozzle region) are divided into two regions for refinement to conduct a grid independence verification. The grid independence verification is conducted under conditions without the cavitation model, with the rotor spinning at 20000 rpm and a vehicle speed of 60 knots, and at 1 atmosphere of pressure. The performance data, including the head and torque of the pump-jet propulsor, are compared to ensure accuracy. The data from the simulation with the worst grid are used as the initial reference. The specific details are presented in Table 2.

As indicated by the data in Table 2, the computational errors for the last three grid combinations are less than 1%, which meets the requirements for numerical computations. Therefore, this paper employs a total of 2882491 grid cells for the internal flow field and 5803248 grid cells for the external flow field to conduct the numerical computations.

The Y+ value is crucial for simulation accuracy because it affects the calculation of the wall shear stress and turbulent viscosity, influencing the overall flow prediction accuracy. Here, we present the Y+ distributions in the areas of the rotor and stator blades, where the flow is most complex and cavitation is most likely to occur. The values are generally less than 50, which can ensure the accuracy of flow prediction. The Y+ values for the rotor blades and the stator blades are shown in Fig. 4.

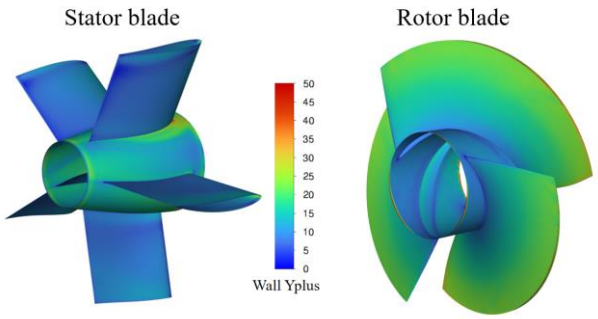

Fig. 4. Blade Y+ values

4. NUMERICAL SETTINGS AND EXPERIMENTAL RESULTS

4.1 Numerical Simulation Settings

First, the operational parameters and variables set for this study are introduced, with the specific parameters listed in Table 3.

Table 3 Operational parameters

Launch depth, H_D (m)	Launch speed, V_K (knots)
50	20/30/40/50/60
100	20/30/40/50/60
200	20/30/40/50/60
300	20/30/40/50/60

The physical properties of seawater vary with depth, and the parameters that primarily affect computations include the viscosity, density, saturation vapor pressure, and standard pressure of the seawater at the respective depth. Among these factors, viscosity and density are closely related to temperature. For example, Korson et al. (1969) demonstrated the viscosity of water at different temperatures, and Yaws et al. (1994) proposed a calculation formula for determining the viscosity of compounds at various temperatures on the basis of temperature. However, the temperature distribution varies across major ocean regions, and factors such as the distance from the equator and depth affect the temperature of seawater at different levels. For example, Emery and Dewar (1982) and Cochrane (1958) researched the differences in seawater properties in various waters of the North Pacific and North Atlantic. The saturation vapor pressure also varies with the temperature of the main water region, as shown by J. Huang's research (2018). The saturation vapor pressures of water and ice change with temperature, and the corresponding calculation formulas are provided in this paper.

Clearly, changes in depth affect multiple variables. Therefore, we quantify the data via formulas and average data from the North Pacific. The depths at which the numerical computations are conducted are 50 m, 100 m, 200 m, and 300 m. Among these depths, 200 m marks the

Table 4 Seawater physical properties for computation at various depths

H_D (m)	T (°C)	ν (Pa·s)	ρ (kg/m^3)	P_V (Pa)
50	10.0	0.00140	1025.0	1228
100	5.0	0.00155	1027.5	873
200	3.5	0.00157	1029.0	785
300	2.0	0.00160	1030.0	706

boundary between the middle-water and shallow sea and is a depth where a significant amount of marine biological research has been focused. The primary physical properties of seawater at various depths are tabulated in Table 4.

In the table, H_D represents the launch depth, T represents the temperature, ν represents the viscosity, ρ represents the density, and P_V represents the saturation vapor pressure.

4.2 Experimental Setup and Test Results

Experimental verification is an important part of comparing the accuracy of simulations. Figure 5 shows the layout of the experimental equipment. The device can simulate high-pressure environments and can mimic the pressure conditions found in deeper oceanic regions. The accuracy of the electromagnetic flowmeter in the figure is 0.1%. We also have two pressure monitors at the valve, both with 0.3% accuracy. The speed control accuracy of the motor is 3%. The overall combined uncertainty is approximately 0.6%.

During the experimental uncertainty analysis, we identified the main sources of error as including equipment accuracy, measurement methods, and operational skills. After quantification and calculation from multiple trials, the expanded uncertainty of the final experimental results was assessed to be 5%. This indicates that our measurement results are highly reliable under the given conditions and can provide support for the simulation content.

The test is conducted in a closed pipe circuit, with the main test parameters being head and efficiency. The head value is calculated from the pressures obtained at the inlet and outlet of the pump-jet propulsor. The calculation formula for efficiency is as follows:

$$\eta_0=\frac{\rho g Q H}{2\pi n_S T} \tag{13}$$

where T represents the torque of the pump-jet propulsor rotor ($\mathrm{N}\cdot\mathrm{m}$), Q is the working flow rate of the pump-jet propulsor (m^3/s), and n_s is the rotational speed of the rotor (r/s).

Figure 6 was plotted on the basis of the experimental data, with Fig. 6 illustrating the performance curve versus flow rate when cavitation is not present. In this section, the pipeline's standard pressure is converted into depth H_T, with the unit being meters (m), and the calculation formula is as follows:

$$H_T=\frac{P_T}{\rho g} \tag{14}$$

where P_T represents the standard pressure set in the test. Figure 6 shows the performance variation due to cavitation at the same flow rate. The degree of cavitation on the horizontal axis is represented by the cavitation number, with a smaller cavitation number σ indicating more severe cavitation. The calculation formula for the cavitation number is as follows:

$$\sigma=\frac{P_\infty-P_V}{0.5\rho U_\infty^2} \tag{15}$$

where P_∞ is the inlet steady flow pressure, measured in Pascals (Pa), and where U_∞ is the inlet steady flow velocity, measured in meters per second (m/s).

Figure 6 shows that with increasing pressure, there are slight increases in the head and efficiency. Additionally, as the flow rate increases, there is a significant decrease in the head data, whereas the efficiency reaches its peak at approximately 0.9 times the design flow rate. Figure 6 also indicates that as the cavitation reaches a certain degree, there is a noticeable decrease in performance.

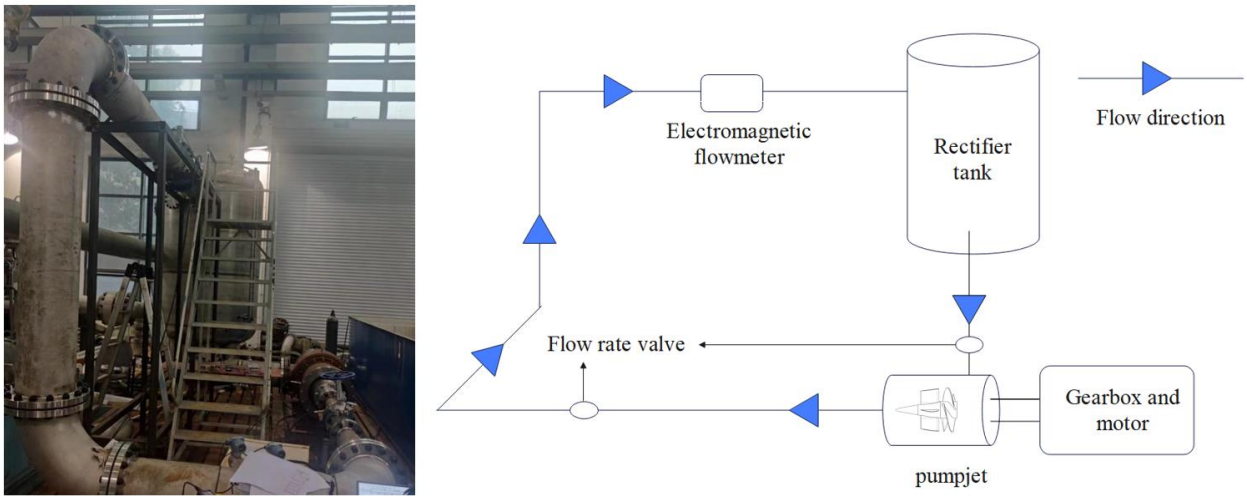

Fig. 5 Experimental design and equipment

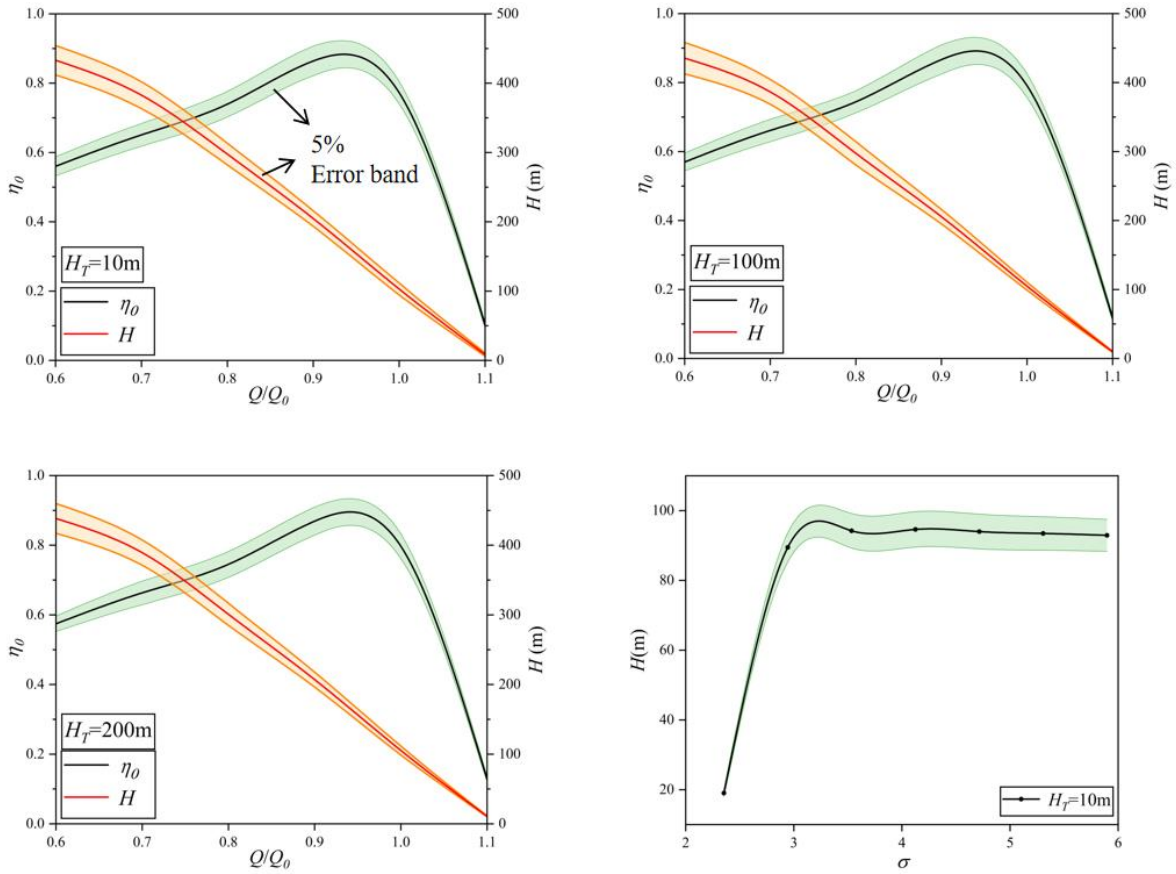

Fig. 6 Experimental data

5. HYDRODYNAMIC AND CAVITATION ANALYSIS

This section primarily investigates the performance of the pump-jet propulsor at various navigation depths and speeds, as well as the cavitation phenomena on the rotor blades.

Table 5 presents the data for the shallow water and mid-water zones when the cavitation model is not activated in the simulation. As indicated by the table, increasing the launch depth results in a slight increase in performance, but the impact is not significant, especially in terms of the rotor thrust coefficient, which is almost negligible. However, a significant decline in performance is observed with increasing launch speed. The above data can be used as a reference for operating conditions under cavitation.

In the table, J represents the advance coefficient, which indicates the level of launch speed. The calculation formula is as follows:

$$J=\frac{V_K}{n_S D_{rs}} \tag{16}$$

A comparison of the thrust for a pump jet propulsor is conducted using the thrust coefficient K_{Tr}.

$$K_{Tr}=\frac{T_r}{\rho {n_s}^2 D_{rs}^4} \tag{17}$$

Table 5 Data for different navigation depths without the cavitation model

H_D (m)	J	H (m)	η_0	K_{Tr}
50	1.1250	97.33	0.640	0.183
	0.9375	101.56	0.655	0.194
	0.7500	106.83	0.672	0.207
	0.5625	110.27	0.678	0.215
	0.3750	113.24	0.684	0.223
300	1.1250	99.55	0.656	0.184
	0.9375	103.079	0.664	0.195
	0.7500	107.13	0.675	0209
	0.5625	111.597	0.683	0.216
	0.3750	115.07	0.689	0.224

In the formula, T_r represents the thrust generated in the rotor and stator regions of the pump-jet propulsor.

Figure 7 presents data with the cavitation model engaged at various launch depths. In general, the performance is notably lower when the cavitation model is turned on than when it is not activated. Examining the data across different launch depths, it is evident that from 100 m to 300 m, there is an overall improvement in performance at launch as the depth increases, with the flow rate stabilizing near the design specification. However, at 100 m, the performance enhancement with speed is more pronounced than that at depths of 200 m and below. Moreover, at high ejection speeds, the performance

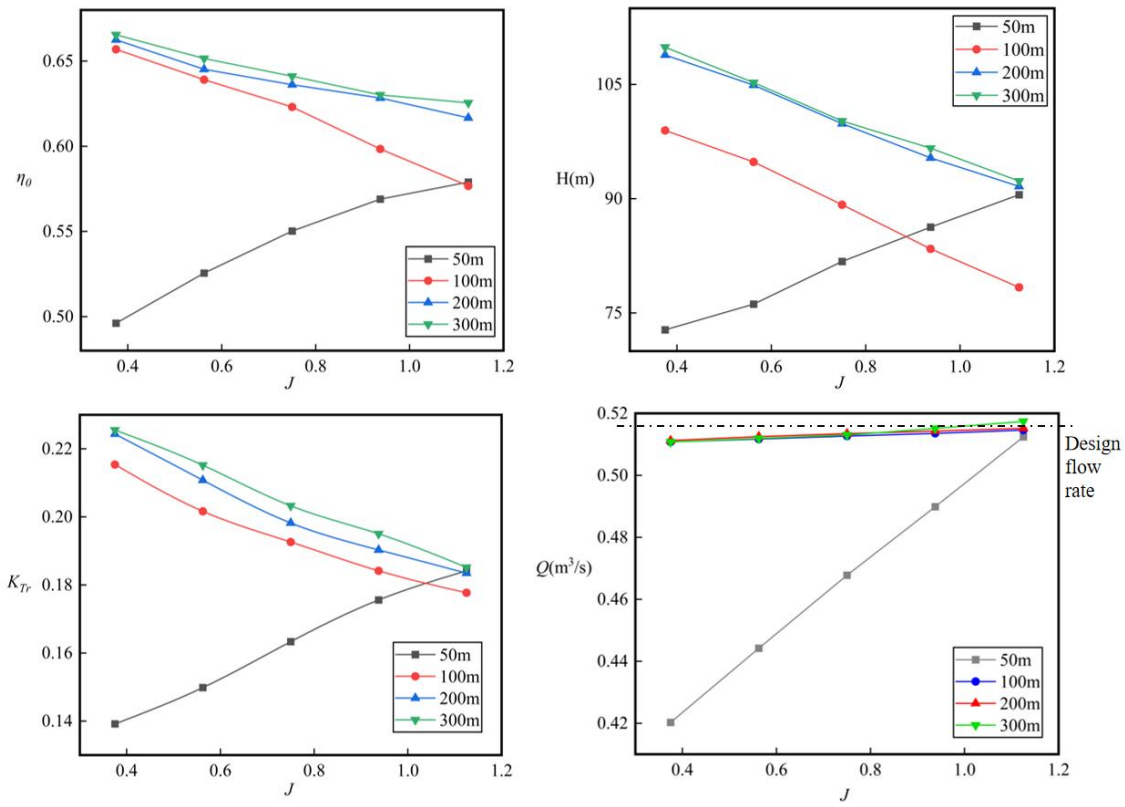

Fig. 7 Cavitation performance data at different depths

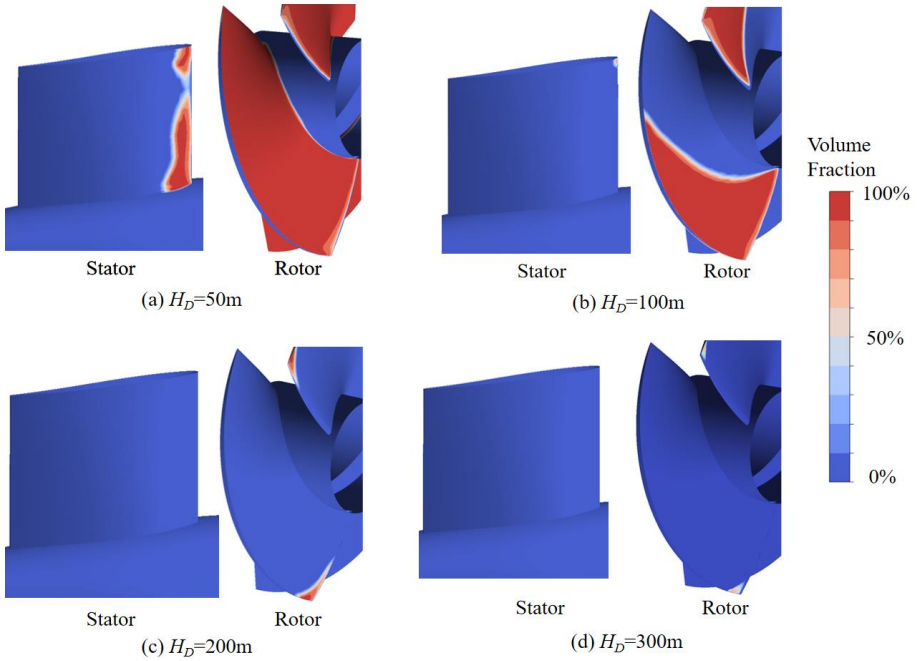

Fig. 8 Cavitation conditions at different depths with *J*=0.375

of the pump-jet propulsor at 100 m is significantly lower than that under non-cavitating conditions.

At a 50 m launch depth, the performance curve stands out from the other curves. Notably, the performance improves markedly with increasing launch speed. At low launch speeds, the flow rate at 50 m is notably below the design flow rate. According to the experimental data, the head should increase as the flow rate decreases, but there is a significant difference when launching at a depth of 50 m. This is most likely related to the internal flow conditions of the pump-jet propulsor. Here we need to understand the flow conditions within the rotor.

Figure 8 shows the cavitation conditions on the rotor blades, guide vanes, and hub of the pump-jet propulsor at different depths with J=0.375. At a launch depth of 50 m, the suction side of the blades is almost completely

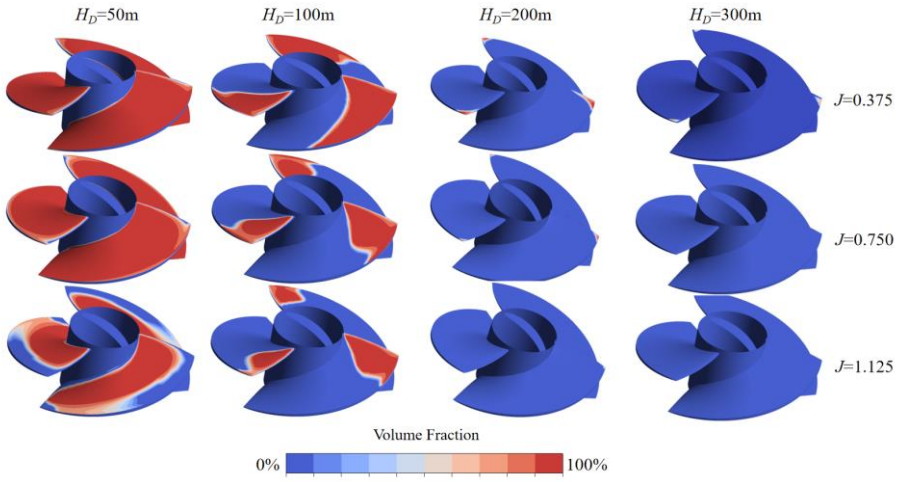

Fig. 9 Impact of the advance coefficient on cavitation at various depths

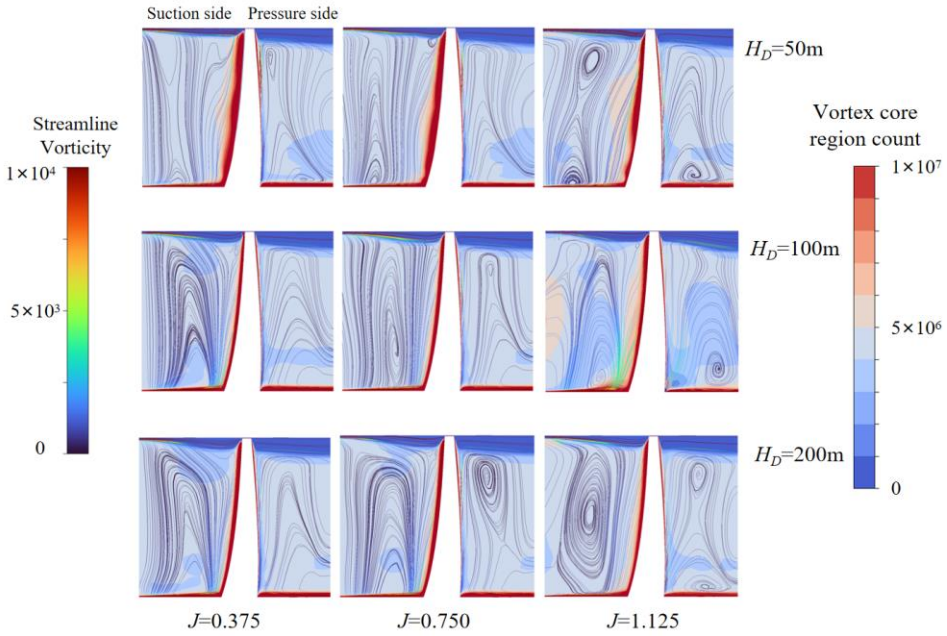

Fig. 10 Cross-sectional diagrams of vortex counts and vorticity streamlines

cavitated, with only a small portion at the leading edge and tip of the blades having less cavitation than the rest of the blades do, and cavitation occurs at the trailing edge of the pressure side. At the same time, cavitation is produced at the leading edge of the stator blades. As the depth increases, the cavitation on the stator blades disappears, and the cavitation on the rotor blades gradually recedes to the leading edge and tip of the blades.

Figure 9 shows the impact of different advance coefficients at the same depth. The observations indicate that as the coefficient J increases, the cavitation condition gradually improves, which is consistent with the data. At a depth of 50 m, the reduction in cavitation extends from the shroud to the hub; similarly, at depths of 100 m to 300 m, the reduction in cavitation also extends from the hub and the middle of the blade to the leading edge and tip of the blade. At depths of 200 m and 300 m, there is virtually no cavitation on the blades from J=0.75 onward, which also verifies that their performance is similar to the simulated data when the cavitation model is not set.

From this, it can be inferred that at a depth of 50 m, under low-speed launch conditions, severe cavitation hinders the internal flow of the pump-jet propulsor, reducing its suction capacity. The poor flow conditions impede the operation of the rotor blades, decreasing the overall performance of the pump-jet propulsor. As a result, the data show a trend of increasing performance with increasing launch speed.

Since the data at 300 m are similar to those at 200 m and no significant cavitation occurs at the rotor, the presentation and description of the 300 m condition are excluded from the following comparison.

Figure 10 shows the vortex counts identified by the Q-criterion and the vorticity streamlines in the axial cross-section of the rotor. The general trend shows that there are two vortex regions with opposite rotation directions on the

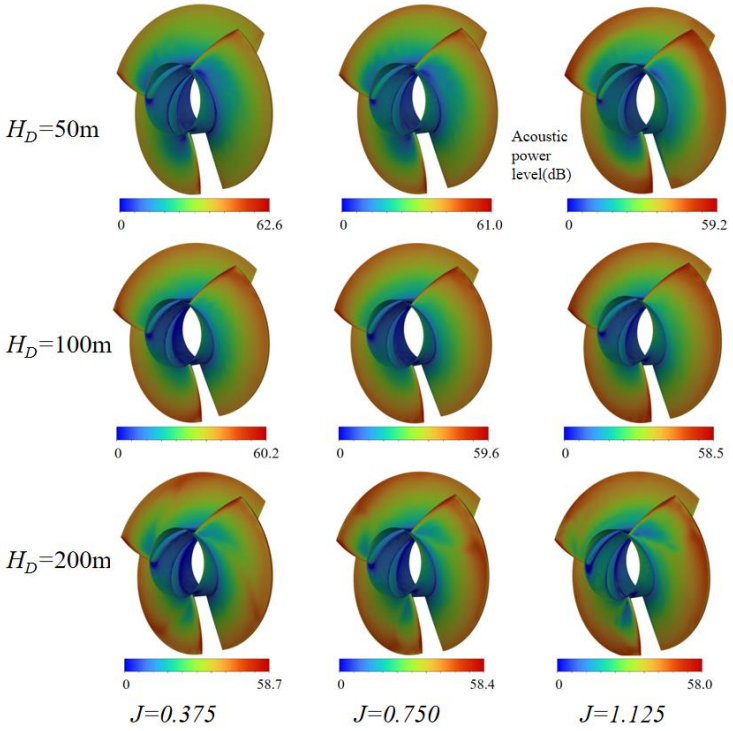

Fig. 11 Sound pressure distributions on the surfaces of the rotor blades

surface of the blades, and these regions separate near the tip clearance. With increasing speed, the number of vortices on the suction side of the blade gradually increases in the middle area of the blade, with increasing vorticity. On the pressure side, they approach the surface of the blade and hub. The areas and intensities of the vortices at the front and rear of the tip-clearance also increase to a certain extent. As the depth increases, the vortices approach the surface of the blade, and the intensities of the vortices above the blade decrease; however, the vortices at the gap are relatively enhanced.

Therefore, according to analysis, increasing the launch depth of the pump-jet propulsor can reduce cavitation, improve internal flow conditions, bring the flow rate back to near the design velocity, and gradually restore the performance to normal. At the same time, an increase in launch speed will lead to a deterioration of the internal flow pattern, causing an increase in vortex strength, which inflicts losses on the performance of the pump-jet propulsor.

6. NOISE ANALYSIS AND INTERACTION ANALYSIS

The data in this part are obtained mainly from transient calculations and steady-state calculations. In the transient calculations, since the rotor standard speed is 20000 rpm, the time it takes for the rotor to complete one rotation is 3×10^{-3} seconds. Therefore, in this work, a time step is defined as a 3-degree rotation of the rotor, which corresponds to 2.5×10^{-5} seconds per step. After the steady-state calculation has stabilized, the IDDES turbulence model is switched to a transient calculation until it stabilizes, and the data from the last two rotations are selected for analysis.

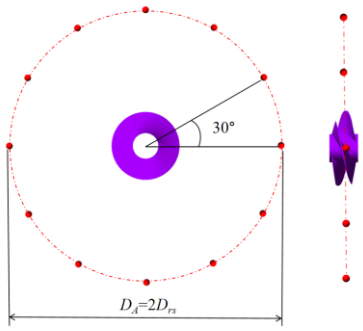

Fig. 12 Schematic diagram of the distribution of the reception points

5.1 Noise Analysis

First, the broad-spectrum sound pressure on the blades is obtained through steady-state calculations, and its distribution is shown in Fig. 11. The main sources of noise on the blade surface are the leading edge and the parts near the shroud, while the noise is close to 0 dB at the hub. With increasing depth, the maximum sound pressure level decreases, but the noise in the middle section of the blade begins to increase and tends to spread toward the middle of the blade. With increasing speed, the maximum sound pressure also decreases, but the maximum sound pressure tends to spread from the rim to the middle section of the blade. The increase in these two variables results in a larger area of high sound pressure on the blade at high launch speeds and deeper depths than at low speeds and shallow depths.

After switching to transient calculations, 12 reception points are established in the computational domain to

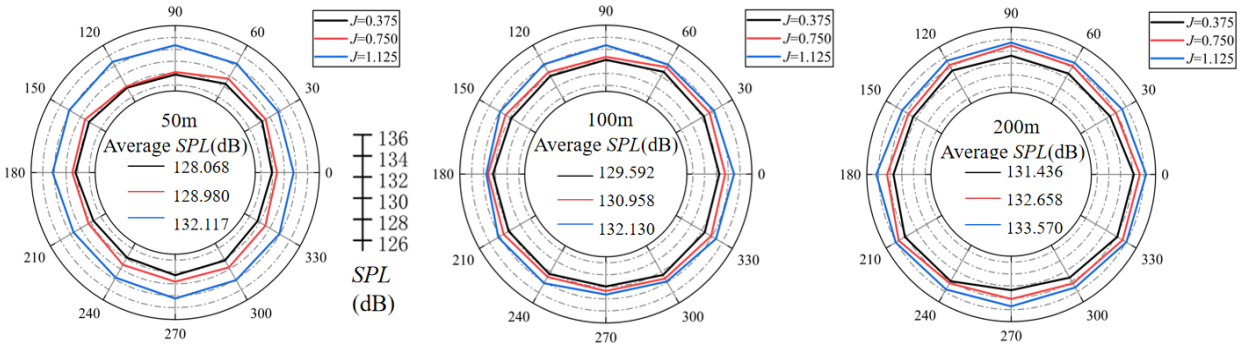

Fig. 13 Total sound pressure level radar charts

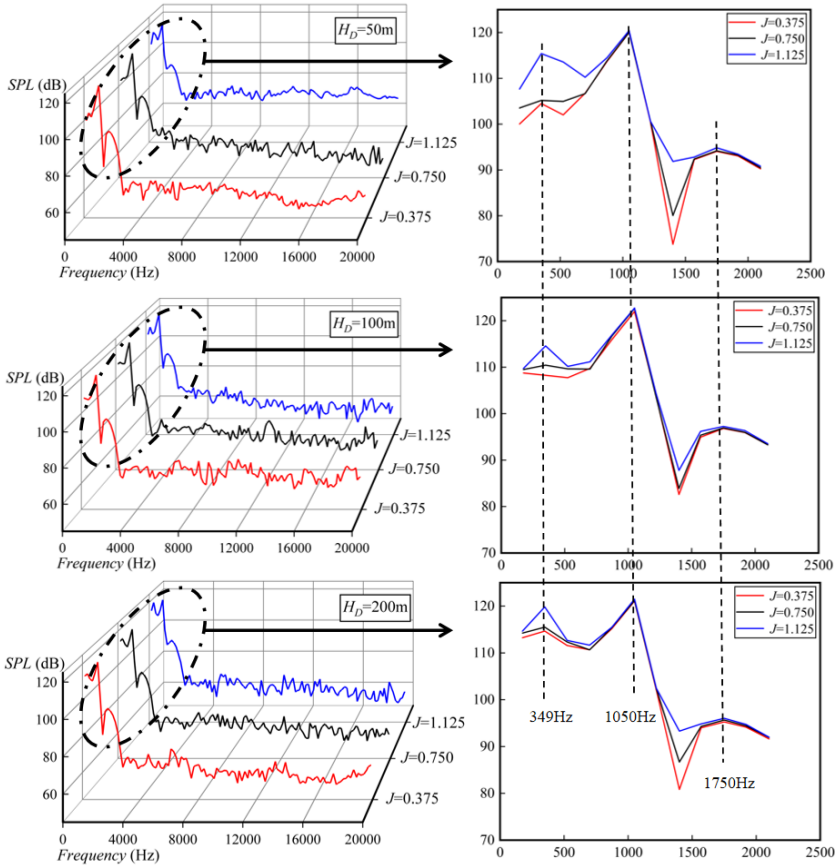

Fig. 14 SPL frequency spectra

monitor the distribution of noise in the radial direction of the rotor. The distribution of the reception points in the computational domain is shown in Fig. 12, with the center of rotation of the rotor as the center and the 12 reception points evenly distributed along the diameter, which is twice D_{rs}, with an interval of 30 degrees between each point.

After processing the total sound pressure distribution obtained from the reception points, the results are shown in Fig. 13. The calculation formula for the sound pressure level (SPL) values in the figure is as follows:

$$SPL=20\log_{10}\left(\frac{p_S}{p_{ref}}\right) \tag{18}$$

where p_s is the sound pressure value at the specified point, p_{ref} is the reference sound pressure, both measured in Pascals (Pa), and the unit for *SPL* is decibels (dB).

As the launch speed increases, the overall sound pressure level also increases. Moreover, as the launch depth increases, the sound pressure level also increases. At a depth of 50 m, the flow rates at high launch velocities exceed those at low velocities, resulting in notably higher noise levels produced by the water flow compared with the quieter conditions at low-speed launches.

Additionally, the processed sound pressure frequency spectrum data are shown in Fig. 14, which were obtained by calculating the average value at each point. As shown in the figure, the maximum *SPL* occurs in the low-

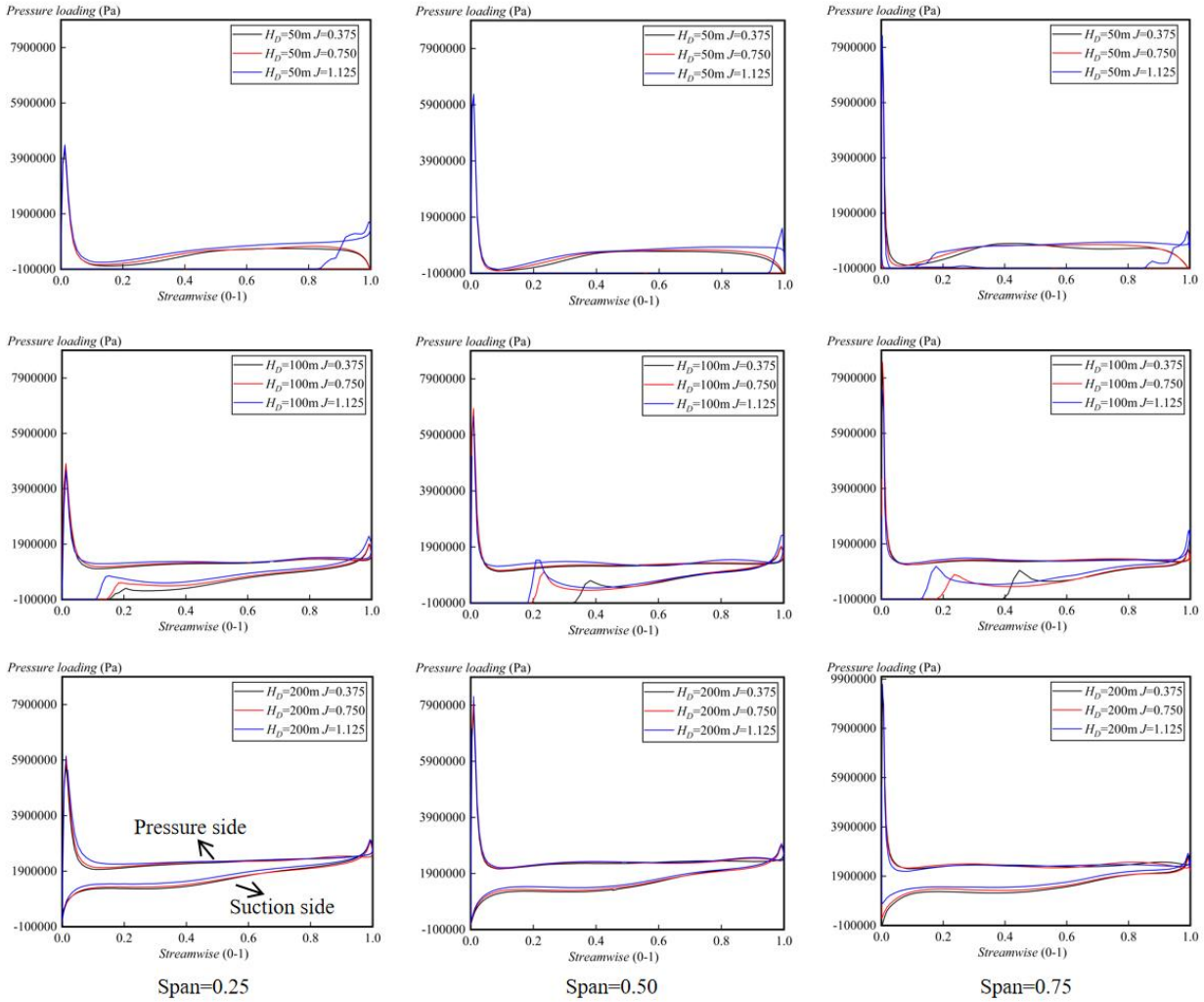

Fig. 15 Blade load distributions along the streamline

frequency range, with the highest peak occurring at 1050 Hz, and as the speed increases, the maximum *SPL* also increases. As the speed increases, the *SPL* values at 349 Hz and 1750 Hz significantly increase. Overall, the *SPL* remains in a stable range after 4000 Hz, generally below 80 dB. Analysis reveals that the noise changes caused by cavitation are manifested primarily in the low-frequency range.

5.2 Blade Structure Analysis

As shown in Fig. 15, along the streamline direction at different spans of the blade, there is a significant change in pressure, with the main load distribution occurring at the leading and trailing edges of the blade. With increasing speed, there is a significant increase in the load at the trailing edge, whereas there is a slight reduction at the leading edge, and an increase in the launch speed causes the positive pressure area on the suction side to gradually move closer to the leading edge of the blade. This phenomenon is due to the improvement in cavitation, which causes the cavitation area to gradually retreat from the middle section of the blade. As the depth increases, the loads on both the suction side and the pressure side of the blade significantly increase. Moreover, with increasing launch depth, the positive pressure zone on the suction side gradually moves closer to the leading edge of the blade. This phenomenon is also closely related to the improvement in blade cavitation.

Transferring the blade loads to the structural mechanics analysis module allows for the determination of the deformation of the rotor blades under the simultaneous influence of torque and fluid. In the structural analysis, the blades are made of structural steel. The parameters of the structural steel are shown in Table 6.

The final results, as shown in Fig. 16, indicate that the maximum deformation of the blade when structural steel is used is 0.10733 mm, occurring at the tip of the leading edge of the blade. As the launch speed increases, the deformation area begins to weaken from the hub. As the depth increases, the amount of deformation in the blade also increases. In the high-speed area at 100 m, the deformation

Table 6 Physical properties of the structural steel

Physical property	Value
Density (kg/m^3)	7850
Tensile yield strength (MPa)	250
Compressive yield strength (MPa)	250
Tensile ultimate strength (MPa)	460

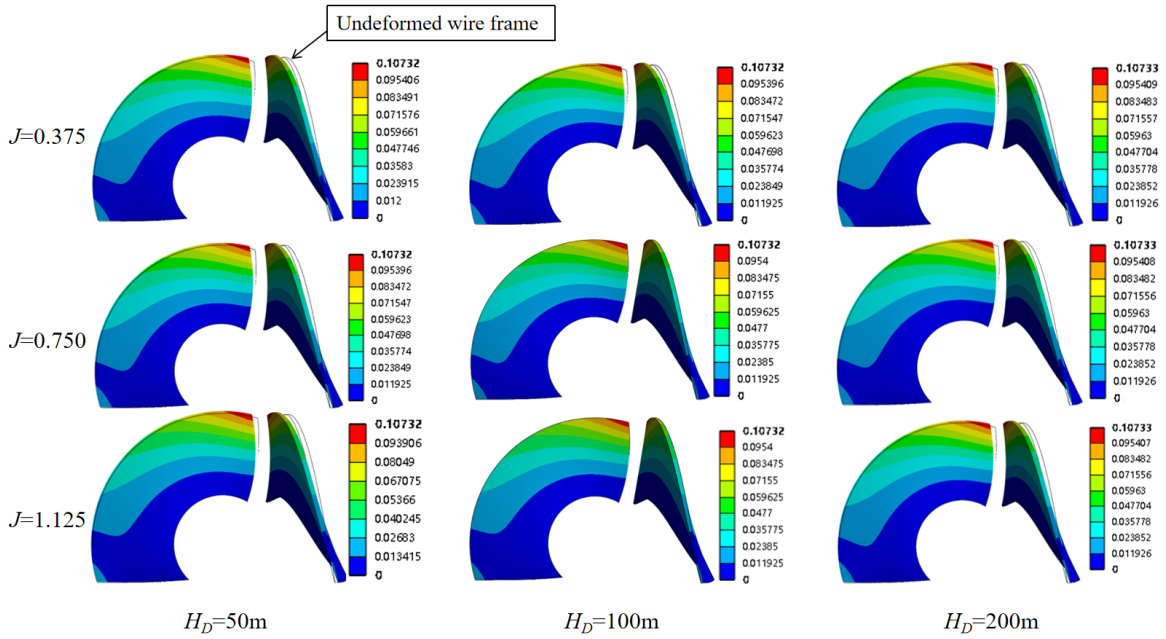

Fig. 16 Blade deformation variation diagram

is greater than that at 50 m because as the speed increases, the degree of cavitation gradually improves, and the increase in the load on the pressure side of the blade supports the deformation caused by water impact and cavitation. At 200 m, although the cavitation conditions are good, the increase in positive pressure on the suction side clearly offsets the support provided by the working face pressure, intensifying the twist of the blade.

6. CONCLUSIONS

This paper investigates the effects of varying the launch depth and speed of a high-speed pump-jet propulsor on the degree of cavitation and its performance. It also explores the effects of the launch depth and speed on the noise generated by the rotor blades and the structural effects on the blades. The specific conclusions are as follows:

1. When cavitation does not occur, increasing the launch depth can enhance the launch performance of the pump-jet propulsor, whereas increasing the launch speed reduces its performance. The shallower the launch depth is, the more severe the cavitation phenomenon; however, increasing the launch speed can mitigate cavitation. Owing to cavitation, the flow rate of the pump-jet propulsor decreases during severe cavitation, leading to a significant drop in performance. In summary, when operating at higher navigation depths, the launch speed can be appropriately reduced to improve performance, whereas near shallow waters, the launch speed should be increased to enhance performance.

2. With increasing launch speed and depth, the maximum sound pressure on the blade surface decreases, but the overall high sound pressure area gradually expands, and the range of high sound pressure spreads from the blade tip to the hub. In the far sound field, increases in speed and depth lead to an increase in the *SPL*. The sound pressure spectrum indicates that the changes in sound pressure due to cavitation originate from the low-frequency range and increase with increasing launch depth and speed. To reduce the noise generated by the rotor during launch, a strategy of launching at a lower depth and a lower launch speed can be adopted.

3. As the launch speed increases, the load on the leading edge of the blade decreases, whereas the load on the trailing edge increases. An increase in launch depth leads to an overall increase in the blade load, and the improvement in cavitation reduces the negative pressure area on the suction side. The main deformation of the blade occurs at the leading edge and the tip. Additionally, an increase in speed reduces blade deformation, whereas an increase in launch depth increases the overall deformation of the blade. Moreover, as cavitation improves, deformation is mitigated.

The research presented in this paper is expected to provide certain data support for subsequent studies, such as investigations of the launch strategy of pump jet propulsors and research on the optimization of pump-jet propulsors. However, this study was limited to calculations at a specific moment and did not consider the entire launch process from acceleration to cruising. The evolution of cavitation and the changes in noise during this period were not addressed. Therefore, in subsequent research, we hope to conduct a detailed study of the entire launch process.

ACKNOWLEDGMENT

We are grateful for the financial support provided by the National Natural Science Foundation of China (52371322).

CONFLICTS OF INTEREST

The authors assert that the contents of this article are not in conflict with any unknown interests of others or organizations.

AUTHOR CONTRIBUTIONS

Qiang Fu: review & editing, supervision, project administration and funding acquisition. **Yuchen Duan**: conceptualization, data curation, formal analysis and original draft. **Wenhao Shi**: validation. **Huairui Li**: validation. **Rongsheng Zhu**: supervision, project administration and funding acquisition.

REFERENCES

Al-Obaidi, A. R. (2018). *Experimental and numerical investigations on the cavitation phenomenon in a centrifugal pump* [Doctoral dissertation, University of Huddersfield].

Al-Obaidi, A. R. (2019). Investigation of effect of pump rotational speed on performance and detection of cavitation within a centrifugal pump using vibration analysis. *Heliyon*, *5*(6). https://doi.org/10.1016/j.heliyon.2019.e01910

Al-Obaidi, A. R. (2023). Experimental diagnostic of cavitation flow in the centrifugal pump under various impeller speeds based on acoustic analysis method. *Archives of Acoustics*, *48*(2), 159-170. https://doi.org/10.24425/aoa.2023.145234

Al-Obaidi, A. R. (2024a). Effect of different guide vane configurations on flow field investigation and performances of an axial pump based on CFD analysis and vibration investigation. *Experimental Techniques*, *48*(1), 69-88. https://doi.org/10.1007/s40799-023-00641-5

Al-Obaidi, A. R. (2024b). Evaluation and investigation of hydraulic performance characteristics in an axial pump based on CFD and acoustic analysis. *Processes*, *12*(1), 129. https://doi.org/10.3390/pr12010129

Al-Obaidi, A. R., & Alhamid, J. (2023). Investigation of the main flow characteristics mechanism and flow dynamics within an axial flow pump based on different transient load conditions. *Iranian Journal of Science and Technology, Transactions of Mechanical Engineering*, *47*(4), 1397-1415. https://doi.org/10.1007/s40997-022-00586-x

Al-Obaidi, A. R., & Alhamid, J. (2024). Analysis of unsteady internal flow characteristics in axial pump with varying number of blades using computational modelling and vibration techniques. *Flow Measurement and Instrumentation*, *99*, 102654. https://doi.org/10.1016/j.flowmeasinst.2024.102654

Al-Obaidi, A. R., Alhamid, J., & Khalaf, H. (2024). Unsteady behaviour and plane blade angle configurations' effects on pressure fluctuations and internal flow analysis in axial flow pumps. *Alexandria Engineering Journal*, *99*, 83-107. https://doi.org/10.1016/j.aej.2024.04.048

Al-Obaidi, A. R., Khalaf, H., & Alhamid, J. (2023a, June). *Investigation of the influence of varying operation configurations on flow behaviors characteristics and hydraulic axial-flow pump performance.* Proceedings of the 4th International Conference on Science Education in The Industrial Revolution 4.0, ICONSEIR 2022, November 24th, 2022, Medan, Indonesia. http://dx.doi.org/10.4108/eai.24-11-2022.2332719

Al-Obaidi, A. R., Khalaf, H., & Alhamid, J. (2023b, June). *Investigation on the characteristics of internal flow within three-dimensional axial pump based on different flow conditions.* Proceedings of the 4th International Conference on Science Education in The Industrial Revolution 4.0, ICONSEIR 2022, November 24th, 2022, Medan, Indonesia. http://dx.doi.org/10.4108/eai.24-11-2022.2332720

An, X., Wang, P., Song, B., & Lessard, L. (2020). Bi-directional fluid-structure interaction for prediction of tip clearance influence on a composite ducted propeller. *Ocean Engineering*, *208*, 107390. https://doi.org/10.1016/j.oceaneng.2020.107390

An, X., Wang, P., Ye, M., He, R., Li, C., & Lessard, L. (2023). Tip clearance influence on hydrodynamic performance and pressure fluctuation of a composite ducted propeller using a two-way FSI method. *Ocean Engineering*, *282*, 114698. https://doi.org/10.1016/j.oceaneng.2023.114698

Cochrane, J. D. (1958). The frequency distribution of water characteristics in the Pacific Ocean. *Deep Sea Research*, *5*(2-4), 111-127. https://doi.org/10.1016/0146-6313(58)90002-9

Dowell, E. H., & Hall, K. C. (2001). Modeling of fluid-structure interaction. *Annual Review of Fluid Mechanics*, *33*(1), 445-490. https://doi.org/10.1146/annurev.fluid.33.1.445

Emery, W. J., & Dewar, J. S. (1982). Mean temperature-salinity, salinity-depth and temperature-depth curves for the North Atlantic and the North Pacific. *Progress in Oceanography*, *11*(3), 219-305. https://doi.org/10.1016/0079-6611(82)90015-5

Ffowcs Williams, J. E., & Hawkings, D. L. (1969). Sound generation by turbulence and surfaces in arbitrary motion. *Philosophical Transactions of the Royal Society of London. Series A, Mathematical and Physical Sciences*, *264*(1151), 321-342. https://doi.org/10.1098/rsta.1969.0031

Gan, G., Shi, W., Yi, J., Fu, Q., Zhu, R., & Duan, Y. (2023). The transient characteristics of the cavitation evolution of the shroud of high-speed pump-jet propulsor propellers under different operating conditions. *Water*, *15*(17), 3073. https://doi.org/10.3390/w15173073

Goossens, M., & Goossens, M. (2003). Fluid equations for mass, momentum and energy. *An Introduction to Plasma Astrophysics and Magnetohydrodynamics*, 59-88. https://doi.org/10.1007/978-94-007-1076-4_3

Gritskevich, M. S., Garbaruk, A. V., Schütze, J., & Menter, F. R. (2012). Development of DDES and IDDES formulations for the k-ω shear stress transport model. *Flow, Turbulence and Combustion*, *88*, 431-449. https://doi.org/10.1007/s10494-011-9378-4

Guo, Z., Xia, W., & Qian, Z. (2022). Study on noise of an axial flow waterjet pump with wavy leading edge. *Ocean Engineering*, *261*, 112117. https://doi.org/10.1016/j.oceaneng.2022.112117

Huang, J., (2018). A simple accurate formula for calculating saturation vapor pressure of water and ice. *Journal of Applied Meteorology and Climatology*, *57*(6), 1265-1272. https://doi.org/10.1175/JAMC-D-17-0334.1

Huang, Q., Li, H., Pan, G., & Dong, X. (2021). Effects of duct parameter on pump-jet propulsor propulsor unsteady hydrodynamic performance. *Ocean Engineering*, *221*, 108509. https://doi.org/10.1016/j.oceaneng.2020.108509

Huang, Q., Qin, D., & Pan, G. (2022). Numerical simulation of the wake dynamics of the pumpjet propulsor in oblique inflow. *Physics of Fluids*, *34*(6). https://doi.org/10.1063/5.0091408

Huang, X., Shi, S., Su, Z., Tang, W., & Hua, H. (2022). Reducing underwater radiated noise of a SUBOFF model propelled by a pump-jet propulsor without tip clearance: Numerical simulation. *Ocean Engineering*, *243*, 110277. https://doi.org/10.1016/j.oceaneng.2021.110277

Korson, L., Drost-Hansen, W., & Millero, F. J. (1969). Viscosity of water at various temperatures. *The Journal of Physical Chemistry*, *73*(1), 34-39. https://doi.org/10.1021/j100721a006

Krappel, T., Kuhlmann, H., Kirschner, O., Ruprecht, A., & Riedelbauch, S. (2015). Validation of an IDDES-type turbulence model and application to a Francis pump turbine flow simulation in comparison with experimental results. *International Journal of Heat and Fluid Flow*, *55*, 167-179. https://doi.org/10.1016/j.ijheatfluidflow.2015.07.019

Li, H., Huang, Q., & Pan, G. (2023). Numerical radiated noise prediction of a pre-swirl stator pump-jet propulsor propulsor. *Journal of Marine Science and Application*, *22*(2), 344-358. https://doi.org/10.1007/s11804-023-00340-y

Li, H., Pan, G., Huang, Q., & Shi, Y. (2020). Numerical prediction of the pumpjet propulsor tip clearance vortex cavitation in uniform flow. *Journal of Shanghai Jiaotong University (Science)*, *25*, 352-364. https://doi.org/10.1007/s12204-019-2138-7

Lu, L., Pan, G., Wei, J., & Pan, Y. (2016). Numerical simulation of tip clearance impact on a pumpjet propulsor. *International Journal of Naval Architecture and Ocean Engineering*, *8*(3), 219-227. https://doi.org/10.1016/j.ijnaoe.2016.02.003

Lu, L., Wang, C., & Qin, D. (2020). Numerical investigations of flow characteristics of a pumpjet propulsor in oblique inflow. *Applied Ocean Research*, *103*, 102343. https://doi.org/10.1016/j.apor.2020.102343

McCormick, B. W., & Elsenhuth, J. J. (1963). Design and performance of propellers and pumpjets for underwater propulsion. *AIAA Journal*, *1*(10), 2348-2354. https://doi.org/10.2514/3.2065

Qin, D., Huang, Q., Pan, G., Han, P., Luo, Y., & Dong, X. (2021a). Numerical simulation of vortex instabilities in the wake of a preswirl pumpjet propulsor. *Physics of Fluids*, *33*(5). https://doi.org/10.1063/5.0039935

Qin, D., Huang, Q., Shi, Y., Pan, G., Shi, Y., & Dong, X. (2021b). Comparison of hydrodynamic performance and wake vortices of two typical types of pumpjet propulsor. *Ocean Engineering*, *224*, 108700. https://doi.org/10.1016/j.oceaneng.2021.108700

Qiu, C., Huang, Q., Pan, G., Shi, Y., & Dong, X. (2020). Numerical simulation of hydrodynamic and cavitation performance of pumpjet propulsor with different tip clearances in oblique flow. *Ocean Engineering*, *209*, 107285. https://doi.org/10.1016/j.oceaneng.2020.107285

Qiu, C., Pan, G., Huang, Q., & Shi, Y. (2020). Numerical analysis of unsteady hydrodynamic performance of pump-jet propulsor propulsor in oblique flow. *International Journal of Naval Architecture and Ocean Engineering*, *12*, 102-115. https://doi.org/10.1016/j.ijnaoe.2019.10.001

Ren, Y., Zhu, Z., Wu, D., Li, X., & Jiang, L. (2019). Investigation of flow separation in a centrifugal pump impeller based on improved delayed detached eddy simulation method. *Advances in Mechanical Engineering*, *11*(12), 1687814019897832. https://doi.org/10.1177/1687814019897832

Shi, S., Huang, X., Rao, Z., Su, Z., & Hua, H. (2022). Numerical analysis on flow noise and structure-borne noise of fully appended SUBOFF propelled by a pump-jet propulsor. *Engineering Analysis with Boundary Elements*, *138*, 140-158. https://doi.org/10.1016/j.enganabound.2022.02.012

Sun, Y., Peng, H., Liu, W., Guo, J., & Guo, Y. (2022). Comparison of the hydrodynamic performance of front and rear-stator pump-jet propulsor propulsors in an oblique wake under the cavitation condition. *Physics of Fluids*, *34*(3). https://doi.org/10.1063/5.0082769

Xiong, Z., Rui, W., Lu, L., Zhang, G. and Huang, X. (2022). Experimental investigation of broadband thrust and loading noise from pumpjet due to turbulence ingestion. *Ocean Engineering*, *255*, 111408. https://doi.org/10.1016/j.oceaneng.2022.111408

Xu, Z., & Lai, H. (2023). Comparison of cavitation in two axial-flow water jet propulsion pumps. *Processes*, *11*(7), 2137. https://doi.org/10.3390/pr11072137

Yang, C., Sun, C., Wang, C., Yao, H. D., Guo, C., & Yue, Q. (2024). Serration of the duct trailing edge to affect

the hydrodynamics and noise generation for a pump-jet propulsor propulsor. *Physics of Fluids, 36*(1). https://doi.org/10.1063/5.0180347

Yaws, C. L., Lin, X., & Bu, L. (1994). Calculate viscosities for 355 liquids. *Chemical Engineering, 101*(4), 119. Retrieved from https://www.proquest.com/trade-journals/calculate-viscosities-355-liquids/docview/194412912/se-2

Ye, J. M., Sun, D. P., Zou, X. Y., Wu, Y. R., & Xi, P. (2022). Tip flow control performance and mechanism of axial slots in a pumpjet propulsor. *Ocean Engineering, 266*, 112950. https://doi.org/10.1016/j.oceaneng.2022.112950

Yuan, J., Chen, Y., Wang, L., Fu, Y., Zhou, Y., Xu, J., & Lu, R. (2020). Dynamic analysis of cavitation tip vortex of pump-jet propulsor propeller based on DES. *Applied Sciences, 10*(17), 5998. https://doi.org/10.3390/app10175998

Zhao, X., Shen, X., Geng, L., Zhang, D., & van Esch, B. B. (2022). Effects of cavitation on the hydrodynamic loading and wake vortex evolution of a pre-swirl pump-jet propulsor propulsor. *Ocean Engineering, 266*, 113069. https://doi.org/10.1016/j.oceaneng.2022.113069

Zwart, P. J., Gerber, A. G., & Belamri, T. (2004). *A two-phase flow model for predicting cavitation dynamics.* Fifth international conference on multiphase flow (Vol. 152). Japan: Yokohama.